



1 **Marine snow morphology drives sinking and attenuation in the**
2 **ocean interior**

3 **List of Authors:**

- 4 Yawouvi Dodji Soviadan^{1,9,10*} ORCID 0000-0003-0622-5772
5 Miriam Beck¹ 0000-0001-8179-3820
6 Joelle Habib¹ 0000-0001-9604-7927
7 Alberto Baudena¹ ORCID 0000-0002-8890-4324
8 Laetitia Drago^{1,2} ORCID 0000-0002-0054-1734
9 Alexandre Accardo¹ ORCID 0009-0008-9426-2250
10 Remi Laxenaire^{3,8} ORCID 0000-0001-5157-1821
11 Sabrina Speich⁴ ORCID 0000-0002-5452-8287
12 Peter Brandt^{5,6} ORCID 0000-0002-9235-955X
13 Rainer Kiko^{1,5,6} ORCID 0000-0002-7851-9107
14 Stemmann Lars^{1,7*} ORCID: 0000-0001-8935-4531
15
16 1 Sorbonne Université, CNRS, Laboratoire d'Océanographie de Villefranche, UMR 7093 LOV,
17 Villefranche-sur-Mer, France
18 2 Sorbonne Université, UMR 7159 CNRS-IRD-MNHN, LOCEAN-IPSL, Paris, France
19 3 Laboratoire de l'Atmosphère et des Cyclones, LACy, UMR 8105, CNRS, Université de La Réunion,
20 Météo-France, Saint-Denis de La Réunion, France
21 4 Laboratoire de Météorologie Dynamique - IPSL, ENS - PSL, Paris, France
22 5 GEOMAR Helmholtz Centre for Ocean Research Kiel, Kiel, Germany
23 6 Faculty of Mathematics and Natural Sciences, Kiel University, Kiel, Germany
24 7 Institut Universitaire de France, France
25 8 Center for Ocean-Atmospheric Prediction Studies, Florida State University, Tallahassee, FL, USA
26 9 Université de Lomé (TOGO)
27 10 MARBEC, IRD, IFREMER, CNRS, Université de Montpellier, 87 Avenue Jean Monnet, 34200 Sète, France
28

29 * Corresponding authors: Yawouvi Dodji SOVIADAN (syawouvi@yahoo.fr or
30 yawouvi_dodji.soviadan@ird.fr) and Lars STEMMANN (lars.stemmann@imev-mer.fr)
31
32
33
34
35
36
37
38
39
40
41
42
43
44
45
46



47 **Abstract**

48 Simultaneous measurements of marine snow (particles larger than 600 μm) morphologies, estimates of
49 their *in situ* sinking speeds and midwater attenuation in export plumes were performed for the first time using a
50 BGC-Argo float equipped with optical and imaging sensors. The float was deployed and recovered after one year
51 drifting in the sluggish flow regime of the Angola basin. Six consecutive chlorophyll-a and particulate matter
52 accumulation events were recorded at the surface, each followed by an export plume of sinking aggregates.
53 Objects larger than 600 μm were classified using machine learning recognition and clustered into four
54 morphological categories of marine aggregates. Plankton images were validated by an expert in a few broad
55 categories. Results show that different types of aggregates were produced and exported from the different blooms.
56 The different morphological categories of marine snow had different sinking speeds and attenuation for similar
57 size indicating the effect of morphology on sinking speed. However, the typical size-to-sinking relationship for
58 two of the categories and over the larger observed size range (100 μm -few mm) was also observed, indicating the
59 importance of size for sinking. Surprisingly, calculated *in situ* sinking speeds were constantly in the lower range
60 of known values usually assessed *ex situ*, suggesting a methodological effect which is discussed. Moving away
61 from purely size-based velocity relationships and incorporating these additional morphological aggregates
62 properties will help to improve mechanistic understanding of particle sinking and provide more accurate flux
63 estimates. When used from autonomous platforms at high frequency, they will also provide increased spatio-
64 temporal resolution for the observation of intermittent export events naturally occurring or induced by human
65 activities associated with marine Carbon Dioxide Removal.

66 **1 Introduction**

67 Production, transfer to depth, and remineralization of organic particles provide a major pathway for the
68 export of carbon from the ocean's surface to the ocean interior (Volk and Hoffert, 1985). Phytoplankton
69 photosynthesis and zooplankton trophic activities produce, in the sunlit ocean, particulate matter at the basis of
70 marine food webs. Among the different physical and biological processes determining the fate of the production,
71 gravitational sinking is responsible for 90% of the carbon vertical flux (Boyd et al. 2019). The mesopelagic, here
72 taken as the 100-1000 m layer, is also the starting depth for a myriad of processes such as particle fragmentation,
73 packaging and/or respiration by the mesopelagic fauna that impact (mostly reduce) the flux as particle sink (Burd
74 et al., 2010; Giering et al., 2014; Stemmann et al., 2004). The faster the sinking is, the more carbon is carried to a
75 depth where it can be stored for a long time (Boyd et al., 2019; Siegel et al., 2023).

76 In the common paradigm, large (>few 100's μm in size) marine particles were thought to be the main
77 vector of the carbon flux (Alldredge and Silver, 1988; Honjo et al., 1982; Stemmann et al., 2002). However, more
78 recently, other particles' characteristics than size (e.g., porosity, ballasting, geometry) were assessed to be
79 important in setting the flux (Cael et al., 2021; Iversen and Lampitt, 2020; Stemmann and Boss, 2012; Williams
80 and Giering, 2022). Particles are often found in the form of aggregates composed of various lithogenic or biogenic
81 elements (Alldredge and Silver, 1988) and their sinking speed depends on the morphological properties of the
82 individual aggregates (size, density, geometry) which depends on the nature of the producers and the
83 aggregation/disaggregation processes (Alldredge and Gotschalk, 1988; Alldredge and Silver, 1988; Iversen and
84 Lampitt, 2020; Ploug et al., 2008a). The efficiency of the deep carbon sequestration depends not only on the
85 aggregates sinking speed but also their attenuation by various mesopelagic processes as they penetrate in the
86 twilight zone of the ocean. A strong vertical flux attenuation in the mesopelagic is usually observed as a result of
87 respiration and particle fragmentation by organisms (Burd et al., 2010; Giering et al., 2014; Stemmann et al.,
88 2004). On one hand, export of fast sinking particles may be less attenuated than slow-sinking ones as they spend
89 less time in this layer but on the other hand, they may be more prone to flux feeding by gatekeeper zooplankton
90 at the base of the mixed layer (Jackson and Checkley, 2011). However, this remains an open question as sinking
91 speed is not only dependent on size (Iversen and Lampitt, 2020) but varies with ballasting (Ploug et al., 2008b, a)
92 and aggregates morphology (Trudnowska et al., 2021) which are barely known.

93 Because the size of particles is easy to measure *in situ* with imaging systems (Gorsky et al., 2000; Picheral
94 et al., 2010, 2022; Stemmann and Boss, 2012) or *ex situ* in experimental design after production or collection
95 (Iversen et al., 2010; Ploug et al., 2010), the majority of previous studies have calculated sinking speeds, from
96 observations or in models, using a power law relationship between sinking and size (Burd, 2023; Forest et al.,



197 2013; Guidi et al., 2008; Iversen et al., 2010; Kiko et al., 2020; Kriest and Evans, 2000; Soviadan et al., 2022;
198 Stemmann et al., 2004). However, the parameters of this size to sinking relationship vary widely as a function of
199 plankton community composition and aggregation processes (Cael et al., 2021; Forest et al., 2013; Laurenceau-
200 Cornec et al., 2015; Stemmann et al., 2004; Williams and Giering, 2022). In some cases, the relationship was not
201 observed (Diercks and Asper, 1997; Iversen and Lampitt, 2020) or showed an opposite pattern (McDonnell and
202 Buesseler, 2010) questioning the nature of the relationship between size and sinking speed or possible bias due to
203 the experimental methods (Williams and Giering, 2022).

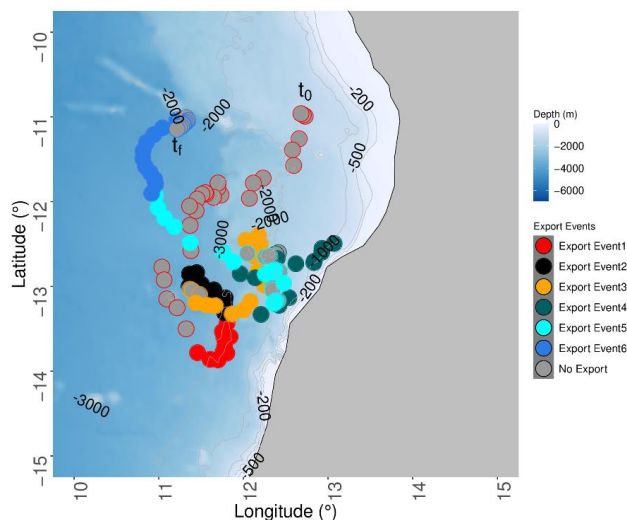
204 Sinking speeds have been generally estimated for decades experimentally, *ex situ*, on collected (or
205 produced) material in 81% of the cases, *in situ* in specific chambers in 14% of the cases and *in situ* by divers in
206 5% of the cases (Cael et al., 2021; Williams and Giering, 2022). More recently, sinking speeds have been
207 calculated by analyzing *in situ* time series of the export plume using optical or camera systems (Briggs et al.,
208 2020; Giering et al., 2020; Stemmann et al., 2002; Trudnowska et al., 2021). There is a debate about whether *in*
209 *situ* or *ex situ* provides accurate estimates of sinking speed because *in situ* ones tend to be lower (Williams and
210 Giering, 2022). Potential bias in *ex situ* experimental design exists due to physical alteration during collection or
211 production, or because the selected particles for experiments do not represent *in situ* particle assemblages
212 (Williams and Giering, 2022). Conversely *in situ* methods provide an estimate of the bulk particle assemblage,
213 possibly sorted as a function of size. The latest advancement in optical and imaging sensor technology have
214 enabled their integration onto autonomous floats (Accardo et al., 2024; Briggs et al., 2020; Lacour et al., 2024;
215 Picheral et al., 2022). Additionally, recent progress in unsupervised image classification now facilitates the
216 classification of individual aggregates into categories (Accardo et al., 2024; Irisson et al., 2022; Trudnowska et
217 al., 2021). When applied to the study of phytoplankton bloom in the Arctic Ocean, the image classification of the
218 different types of detritus obtained using the Underwater Vision Profiler 5 deployed from a ship, showed, for the
219 first time, a clear relationship between phytoplankton community structure and aggregates morphology with an
220 impact on the sinking aggregate (Trudnowska et al., 2021). Networks of Biogeochemical (BGC)-Argo floats are
221 now deployed with optical sensors to better estimate and understand processes of carbon flux and attenuation
222 (Accardo et al., 2024; Henson et al., 2024; Lacour et al., 2024). Imaging sensors, by providing more qualitative
223 data, will bring a substantial increase in our knowledge of mesopelagic dynamics and the interplay between
224 particles and plankton at scales varying from local to global (Biard et al., 2016; Drago et al., 2022; Laget et al.,
225 2024; Panaiotis et al., 2023; Stemmann et al., 2002, 2008).

226 In this study, we analyze the results of image analysis of a recovered Underwater Vision Profiler 6
227 (UVP6) camera mounted on a BGC-Argo float from May 2021 to April 2022 drifting in the sluggish flow regime
228 of the Angola basin. During the one-year deployment, the float drifted slowly in a region with weak currents and
229 low mesoscale activity. Seven consecutive marine snow production events were recorded at the surface and six of
230 them lead to an export plume of sinking aggregates. Unsupervised classification of all the marine snow aggregates
231 was performed to identify the different types of particles. The objectives of this work are i) to automatically
232 classify *in situ* images of marine snow, ii) to describe the assemblage of marine snow particles at the surface and
233 in the mesopelagic during the six intermittent production and export events and iii) infer marine snow
234 morphotypes sinking velocities and vertical attenuation in the export plume. To our knowledge, this work provides
235 the first estimates of sinking speeds and export attenuation for different types of particulate materials recorded
236 from a BGC-Argo float.



137 2 Methods

138 2.1 BGC-Argo float deployment



139 **Figure 1: Angola region of the BGC-Argo float deployment with the trajectory during the one-year drift. The filled**
140 **dots correspond to the 6 export events and the colors of unfilled dots indicate the period before each export event in**
141 **the same color except for the last period for which it indicates after the export. The beginning (11° S, 12°45' E noted**
142 **t₀) of the period before the export event1 indicates the float position at its deployment and the end of (11°10' S, 11°13'**
143 **E noted t_f) the period after export event6 indicates the position at its recovery.**
144

145
146 The BGC Argo float (WMO:6903096) was deployed on 4 May 2021 at 11° S, 12°45' E during RV Sonne cruise
147 SO283 and retrieved on 26 April 2022 at 11°10' S, 11°13' E during RV Meteor cruise M181. Distance between
148 surfacing every three days was on average 16 km +/- 11.73 with 4 periods (May 2021, June 2021, December 2021,
149 February 2022) when the drift could reach 40 km in three days. In general the bathymetry was deeper than 1000
150 m (Fig. 1). The general pattern of the drifting was toward south, almost reaching 14° S in August 2021, then north-
151 eastward toward the isobath 700m depth which was reached in early December 2021. Thereafter, the float drifted
152 toward south-west along the isobath 700m until the end of December 2021. The float drifted away from the coast
153 toward north up to the latitude 11° N at which it was recovered.

154 2.2 Environmental and satellite data

155 2.2.1 Float data (CTD, Chla, Bbp)

156 The float was equipped with several sensors to characterize the properties of the water column. First, to
157 measure hydrological parameters, the float was fitted with pressure (DRUCK_2900PSIA, SN: 11587115),
158 temperature, and salinity sensors (SBE41CP_V7.2.5, SN: 13100). Second, to measure biogeochemical properties,
159 it was equipped with oxygen (AANDERAA_OPTODE_4330, SN: 3489), fluorescence (proxy for Chla) and
160 backscattering (700 nm, referred as Bbp taken as a proxy for all suspended particles ap.<10 μm) sensors
161 (ECO_FLBB_2K, SN: 6310). Fluorescence and backscatter were converted to units of Chla (mg m⁻³) and
162 particulate organic carbon (POC, mgC m⁻³) as in Accardo et al. (2024). The UVP6 (SN: 101LP) was mounted on
163 the float. All the data were recorded during the ascent of the float, and are made freely available by the
164 International Argo Program (<https://fleetmonitoring.euro-argo.eu/float/6903095>, link accessible on 06/11/2024).



165 2.2.2 Satellite data (SSH, Lagrangian diagnostic)

166 Several Lagrangian diagnostics were computed at each profile location using velocity data and
167 environmental satellite products. Firstly, for each station (*i.e.*, profile location) a region considered as
168 representative of the water column sampled by the float was defined. This region, in this study, was a circular
169 neighborhood of radius r of 0.1° around each exact profile location. Then, this circular shape was filled with virtual
170 particles at the surface separated by 0.01° (resulting in ~ 300 particles). Afterward, the next step was to compute
171 for each virtual particle several Lagrangian diagnostics. This led to about 300 values for each sampling station
172 which were averaged together, providing a given diagnostic around each profile location. The choice of using a
173 circle around the float profiling location is done to smooth the errors associated with the velocity field uncertainty,
174 as shown in previous studies (Baudena et al., 2021; Chambault et al., 2019; Ser-Giacomi et al., 2021). The velocity
175 field used was derived from both altimetry and assimilation model delayed-time data and includes the geostrophic
176 and the Ekman components (Copernicus Marine Environment Monitoring Service (CMEMS) product
177 MULTIOBS GLO PHY REP 015 004-TDS). It was used to advect each virtual particle (within the representative
178 water parcel) from the profile day until an advective time (τ) ranging between 5 and 45 days backward in time.
179 For each advective time, a diagnostic mean value was available for each profile. Diagnostics were numerous, so
180 only those which provided significant results will be developed here. The first one used was the Finite-Time
181 Lyapunov Exponents (FTLE, days⁻¹). This metric is useful to identify frontal features (Baudena et al., 2021). In
182 this study, a front is defined as a physical barrier at the surface that separates two water volumes of different
183 hydrographic properties that likely were very far from each other in the previous days. FTLEs were calculated as
184 in (Shadden et al., 2005) and the main parameter that was considered was the initial separation between two virtual
185 particles. The second diagnostic used was the Lagrangian chlorophyll-a (mg m^{-3}), *i.e.*, the mean chlorophyll
186 content along the backward particle trajectory. These metric estimations were computed thanks to satellite data of
187 surface chlorophyll-a concentrations which was provided by CMEMS Copernicus website (delayed-time satellite
188 product “OCEANCOLOUR GLO BGC L4 MY 009 104-TDS”).

189 2.3 Particle data taken by UVP6

190 2.3.1 A broad size classification of all particles into two size categories

191 A broad size classification was applied on raw size particles spectra data ($>100 \mu\text{m}$ up to few mm)
192 provided by the UVP6 (without any plankton identification). In this case the assumption was made that
193 zooplankton represent only a small fraction of objects sampled by the UVP6 compared to particles. Then, size
194 range was divided into two sub-classes: MiP (Micrometric Particles) integrating the concentrations over all size
195 classes between 0.1 and 0.5 mm and MaP (Macroscopic Particles) integrating the concentrations of size classes
196 between 0.5 and 16 mm. This lower threshold was used because it corresponds to the definition of marine snow
197 (Alldredge and Silver, 1988). The vertical flux of these two categories was calculated assuming an empirical
198 relationship to convert particle size to POC and another one to obtain sinking speed from size (Kriest, 2002) (with
199 reference 2a of Table 1 and reference 9 of Table 2 for mass and sinking speed of a particle) and previously used
200 in the inter tropical Atlantic Ocean (Kiko et al., 2017, 2020).

201 2.3.2 Unsupervised morphological classification of marine snow in four categories

202 An unsupervised classification method was applied, following an approach previously used to study
203 marine snow in the Arctic Ocean (Trudnowska et al., 2021) and in the Southern Ocean (Accardo et al., 2024).

204 Prior to the analysis, zooplankton and particle images were separated by supervised classification and
205 treated independently. The first step consists in summarizing the 27 morphological features that were derived
206 from the individual particle images. Those features (Table S1) describe their size (e.g., area, perimeter), shade
207 intensity (e.g., mean/median gray level), shape (e.g., symmetry, elongation), and structure (e.g., homogeneity or
208 heterogeneity, mostly based on the variability in gray level). To reach a normal distribution of each variable,
209 extreme values (below or above the 5th and 95th percentile) were flagged as NA - which is interpreted neutral by
210 the following methods - before applying the Yeo-Johnson transformation (Yeo and Johnson, 2000). These traits



211 were then summarized via dimensionality reduction using Principal Component Analysis (PCA). The PCA
212 function scales the features to unit variance prior to the analysis and creates a multi-dimensional “morphospace”
213 in which each particle was positioned based on its morphological features. As in the work of (Trudnowska et al.,
214 2021), size turned out to be the main morphological trait. Therefore, we repeated the same procedure by removing
215 all size-related features (-area, -perim., -major, -feret, -convperim, -skeleton_area, -convarea_area, -
216 symetrieh_area, -symetriev_area, -elongation) to hopefully better distinguish the particles by their other
217 morphological traits. To assess the sensitivity of this classification we also tested alternative algorithms within
218 this approach (see section Sensitivity of aggregates classification to the method in Supp. Mat.). In particular, we
219 tested UMAP (McInnes et al., 2018), a method of dimensional reduction to define the morphospace. In contrast
220 to PCA which creates a linear projection, UMAP is a non-linear dimensional reduction method that has been used
221 previously in similar contexts (Stolarek et al., 2022; Teixeira et al., 2022). To ensure comparability with the PCA,
222 data was scaled prior to the application and four axes were retained to define the morphospace. All other
223 parameters were kept with the same default values (n_neighbors=15, min_dist=0.1) since the resulting
224 morphospace separated the particles as expected.

225 The second step, the classification, was the same for all options (PCA/ UMAP, with/ without size-related
226 features). A k-means clustering was performed on the particles’ coordinates on the first four principal components
227 of a morphospace. The number of clusters (“k”) was set to four, a value which in several simulations conducted
228 the best trade-off between partitioning into visually clearly distinct groups of particle morphology and simplicity
229 in the following analysis. See section Marine snow classification in Supp. Mat. for a test of k=5 and 10 to assess
230 the impact of this choice on the result. Finally, the concentration (nb m⁻³) of each morphotype was computed by
231 dividing the number of particles found in each depth bin by the volume sampled by the UVP6. To study their
232 spatio-temporal distributions, group concentrations were interpolated according to depth and time with a
233 resolution of 5 meters and one day respectively.

234 **2.4 Data analysis**

235 **2.4.1 Sinking speed and particle vertical attenuation**

236 We calculated the sinking speed for six export plumes that were detected by successive peaks at different
237 depths (Fig 2). Assuming constant sinking velocity in the upper 1000m and a Lagrangian drift in a weak vertical
238 shear environment during the short marine snow production events (on average <1 month), we followed the
239 published method developed to survey the evolution of export plumes developed for optical and imaging systems
240 (Briggs et al., 2020; Lacour et al., 2024). In this vertical binning approach more appropriate for large particles, a
241 Gaussian fit is applied to the median concentration of different aggregate size classes per 100 m depth bins. For
242 each size class and type of marine snow, a linear regression was done on the coordinates in depth and time of each
243 of the Gaussian fits’ maximums. The value of the slope and the concentrations of the particles at the different
244 depths were stored if the Gaussian fit was successful for at least 3 depth layers. The slope is an indicator of the
245 sinking speed, while the particle vertical gradients were modeled using a power law model ($N(z)=N_{100} \cdot (z/100)^{-b}$)
246 with a reference depth at 100 m to retrieve the *b* exponent as an indicator of particle attenuation. This method was
247 initially proposed for POC flux measured in sediment traps (Martin et al., 1987) and vertical flux obtained with
248 profiling cameras (Guidi et al., 2008, 2015), but here it was applied to aggregate concentrations in export plumes
249 as in (Trudnowska et al., 2021). Due to the non-sinking behavior or because of the low signal-to-noise ratio in the
250 upper size range where particles are rare, this approach did not work for all size classes in all categories.

251 Finally, sinking speeds as a function of size and aggregate types were also calculated over the whole
252 deployment with lagged correlation between time series in two different depth layers (0-100 and 300-400 m). The
253 lag with the maximum correlation indicates the time for the different particle communities to sink from the upper
254 layer to the deeper layer (average distance of 300 m).

255 **2.4.2 Canonical Redundancy Analysis (RDA) of particle assemblage**

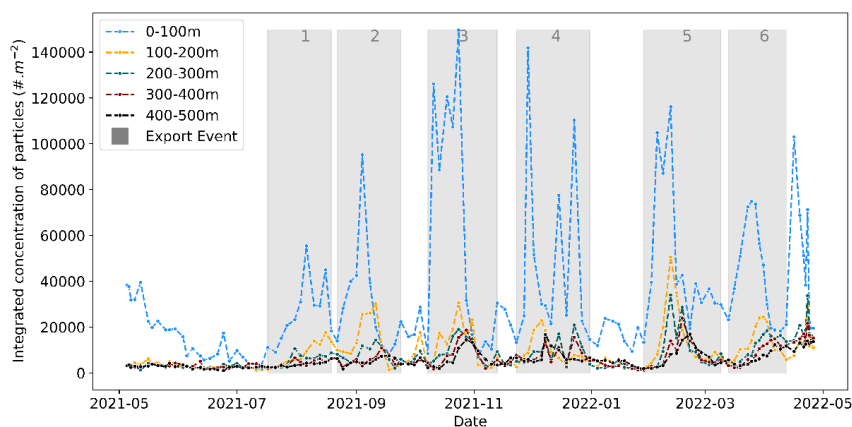
256 For each depth layer, a canonical redundancy analysis (RDA) was performed based on the abundances
257 of the 4 marine snow morphotypes and the above-mentioned environmental variables to explore the explanatory



258 power of these variables in structuring marine snow. The RDA is an extension of the multiple regression analysis
259 applied to multivariate data (Legendre and Legendre, 2012). It allows representing the response variables
260 (abundances of the 4 categories) in a “constrained” reduced space, i.e., constructed from the explanatory variables
261 (the environmental variables). For each RDA, the following variables were used as “supplementary variables” of
262 the analysis to visualize their correlation with the environmental structuring of marine snow assemblage (i.e., to
263 visualize their position in the RDA space). Beforehand, a Hellinger transformation was performed on the
264 abundances in order to reduce the impact of large concentration values. Significant axes were identified using the
265 Kaiser-Guttman criterion (Legendre and Legendre, 1998).

266 2.4.3 Identification of intermittent production and export events in a marine snow time series

267 We determined the marine snow production and export events using their time series in 5 depth layers
268 (Fig. 2). Major peaks were found in the different layers at a few months intervals. Except for the first surface peak
269 (0-100 m) in May 2021, the subsequent six surface particle peaks were followed by peaks in the mesopelagic layer
270 (noted 1 to 6 in Fig. 2). The beginning of each period was set at the start of marine snow accumulation in the first
271 layer and the end was set at the time of the subsequent minimum in the deeper layers. Throughout the manuscript,
272 we will refer to these six events as “plumes” or “events”.

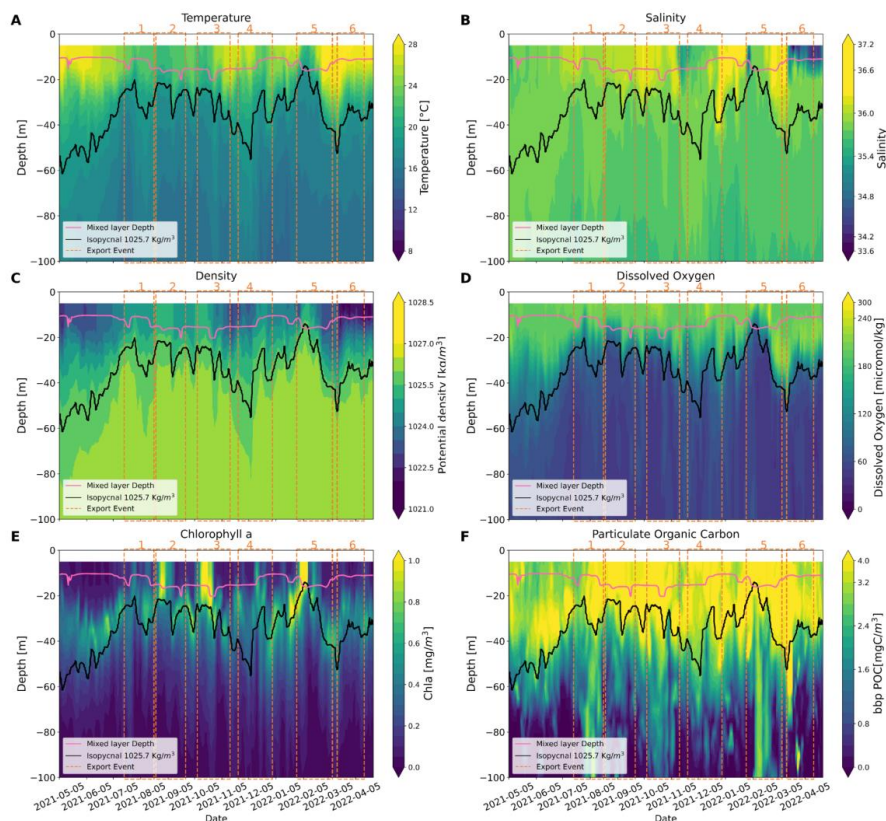


273
274 **Figure 2 : Time series of vertically integrated marine snow (MaP, all particles >600µm) concentrations (# m⁻²) in 5**
275 **layers in the upper 1000 m depth. The 6 bloom periods shaded in gray correspond to six export events that are marked**
276 **by delayed peaks in the mesopelagic. The periods are defined for the events in 2021 as 07/17-08/19, 08/22-09/24, 08/10-**
277 **11/13, 11/23-12/31 and in 2022 as 01/28-03/09 and 03/13 to 04/12.**



278 **3 RESULTS**

279 **3.1 Epipelagic time series of hydrological and biogeochemical properties**

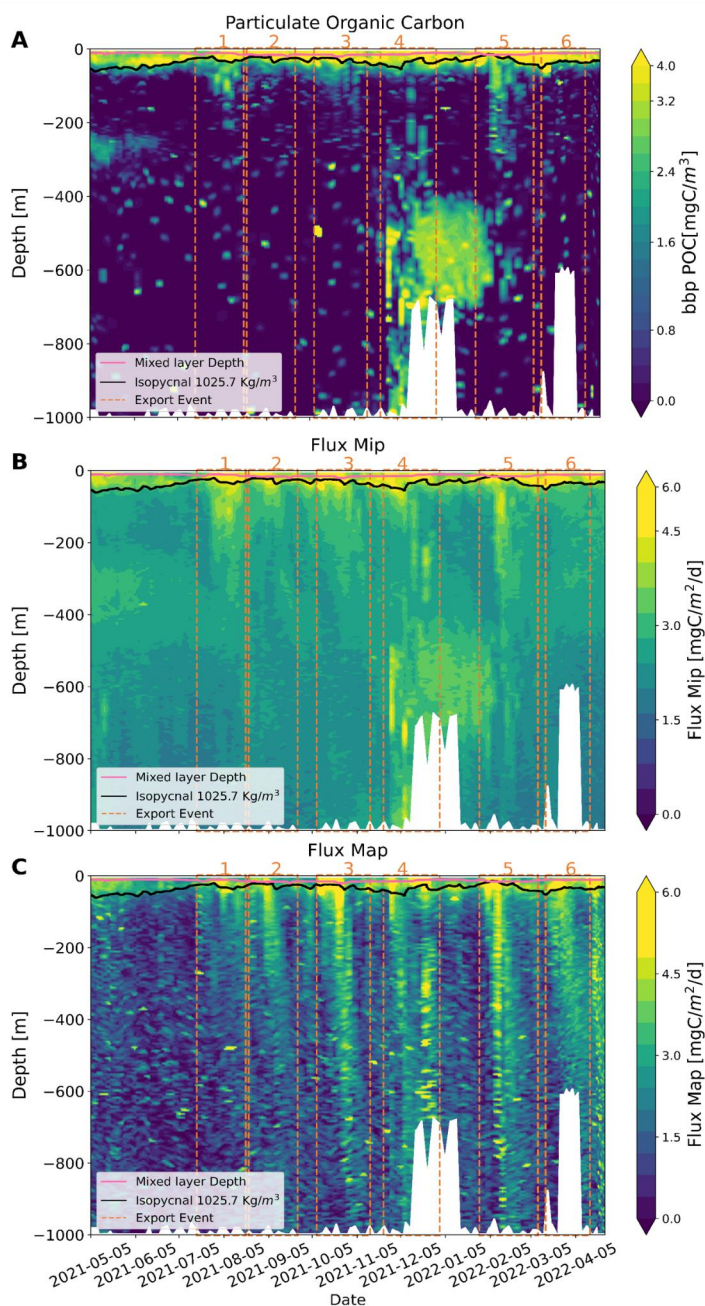


280
281 **Figure 3 : 0-100 m, 2D time series of A) temperature, B) salinity, C) density, D) dissolved oxygen, E) chlorophyll *a***
282 **concentration and F) Bbp POC. The black line depicts the 1025.7 kg m⁻³ isopycnal. The red line represents the mixed**
283 **layer depth.**

284 Sea surface temperature showed the lowest temperatures (21-23°C) from July to September 2021, with
285 the highest temperatures recorded in March and April 2021 (up to 28°C) (Fig. 3). Sea surface salinity exhibited
286 low values in November 2021 (<35) and particularly from March to April 2022 (<34.2). Densities within the
287 upper 30 m depth showed their lowest values from May to June, from mid-October to December 2022, and after
288 February 2022. The isopycnal 1025.7 kg m⁻³ used as an indicator of upwelling (Körner et al., 2024), was shallow
289 (20-30m) between July and October 2021, and as well as from December 2021 to mid-February 2022. It reached
290 its maximum depth in May-June, December 2021 and early March 2022. Highest Chla concentrations were always
291 found in the upper 30 m with an important deep chlorophyll maximum (DCM) around 30-40 m depth. The DCM
292 oscillated within this depth range following the rise of the 1025.7 kg m⁻³ isopycnal, displaying periods of
293 intensification along with an upward movement towards the surface (notably in August, October 2021, and
294 February 2022 concomitantly to the export periods 2, 3 and 5). From May to July 2021, the peak of small particles
295 or bbp followed the DCM but thereafter to the end of the deployment (May 2022) extended from the surface down
296 to the isopycnal 1025.7 kg m⁻³. During three periods of strong export (periods 1, 3 and 5), elevated Bbp (>3 mgC
297 m⁻³) were observed extending down to a depth of 100 m.



298 **3.2 Full Depth (0-1000m) time series of Bbp, MiP and MaP**



299
300
301
302
303

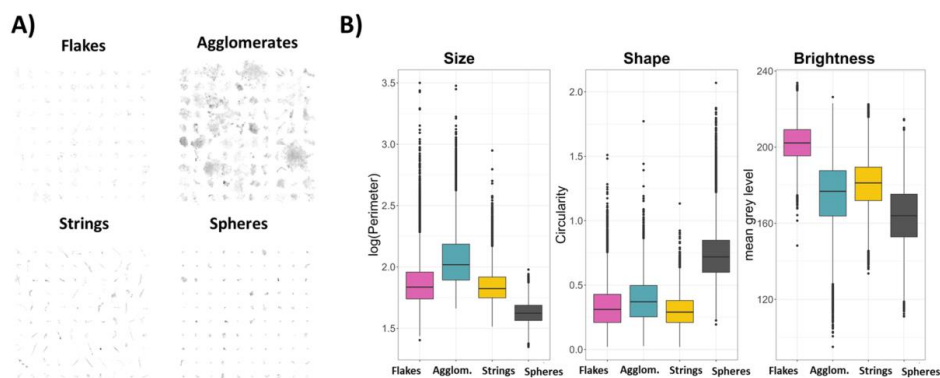
Figure 4: Time–depth profiles determined from the BGC Argo float for A) Bbp, B) MiP flux, and C) MaP flux (in logarithmic scale) as a function of time and depth with the 6 export periods being illustrated by the red vertical dashed lines. The black line depicts the 1025.7 kg m^{-3} isopycnal. The maximum depth of the float that corresponds to the bottom depth has been overlaid as a white mask. The red line represents the mixed layer depth.



304 Small particles detected by the Bbp sensor (few μm) and the MiP ($0.1 < \text{ESD} < 0.5 \text{mm}$) flux detected by
305 the UVP6 showed remarkably similar temporal patterns with different vertical extensions notably during the
306 export events. They showed all along the deployment highest values in the upper 100 m depth (Fig. 4 a-b). A
307 distinct midwater peak was observed from May to June 2021 between 250 and 300 m depth for Bbp and from 300
308 to 400 m for MiP. Very high Bbp ($>20 \text{mgC m}^{-3}$) and MiP ($>20 \text{mg C m}^{-2} \text{d}^{-1}$) were observed from 400 to 600 m
309 depth at the time when the float was in a shallow region in December 2021. Apart from this deep occurrence, the
310 Bbp vertical extent reached 250 m at maximum during periods 1, 3 and 5. The MiP penetrated deeper in the water
311 column down to 300 m depth during all export periods (albeit more in periods 1, 2, 3 and 5, August, October and
312 December 2021, February 2022 respectively).

313 In contrast, large particles as indicated by the MaP ($>500 \mu\text{m}$) flux showed a distinct spatio-temporal
314 pattern, with the highest values occurring in the upper 100 m depth ($100\text{-}400 \text{mgC m}^{-2} \text{d}^{-1}$) differently from the
315 bbp and Mip which showed maximum concentration in midwater layers. Following July 2021, the MaP flux
316 exhibited 6 intermittent events ($>100 \text{mgC mgC m}^{-2} \text{d}^{-1}$ Fig. 4c), during which export plumes showed oblique
317 patterns extending from the surface down to the mesopelagic particularly in August (period 1), September (period
318 2), October (period 3) and December (period 4) 2021 and February (period 5) and April (period 6) 2022. These
319 occurrences, notably in October 2021 and February 2022, reached depths down to 1000 m, leading to a two-fold
320 increase in the computed flux during the export relative to the situation before and after.

321 3.3 Image classification of marine snow $>600 \mu\text{m}$ into four morphotypes



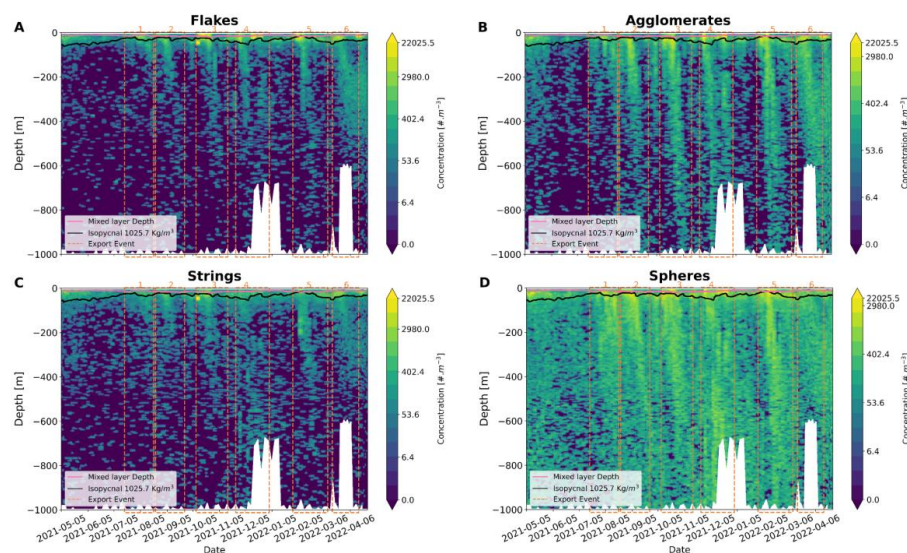
322 **Figure 5: A) Example vignettes of the four defined morphotypes (flakes, agglomerates, strings and spheres) and B)**
323 **their mean morphological traits describing main aspects of size (via perimeter (μm)), shape (via circularity,**
324 **dimensionless) and brightness (via mean gray level, dimensionless range 0 black to 256 white pixel).**
325
326

327 To depict the nature of the sinking aggregates, we classified them performing k-means clustering on the
328 coordinates of particles along the four retained PCA axes. Within this continuous morphospace, we identified four
329 morphotypes (Shown in Fig. 5A), selected as a suitable compromise between contrasted groups and contextual
330 knowledge to explain their nature. Cluster 1 corresponds to medium-sized and bright aggregates named **flakes**
331 (mean perimeter = $1.86 \mu\text{m}$, mean circularity = 0.33, mean brightness = 202.46, Fig. 5). Cluster 2 contains large
332 and dark particles named **agglomerates** (mean perimeter = $2.06 \mu\text{m}$, mean circularity = 0.38, mean brightness =
333 174.91). Cluster 3 contains medium-sized and elongated aggregates named **strings** (mean perimeter = $1.84 \mu\text{m}$,
334 mean circularity = 0.30, mean brightness = 180.69). Cluster 4 is composed of small and circular aggregates named
335 **spheres** (mean perimeter = $1.63 \mu\text{m}$, mean circularity = 0.73, mean brightness = 163.87). More results on marine
336 snow classification and on the sensitivity of aggregates classification to the method is provided in Supp. Mat.).



3.4 Spatio-temporal distribution of marine snow morphotypes (>600 μm)

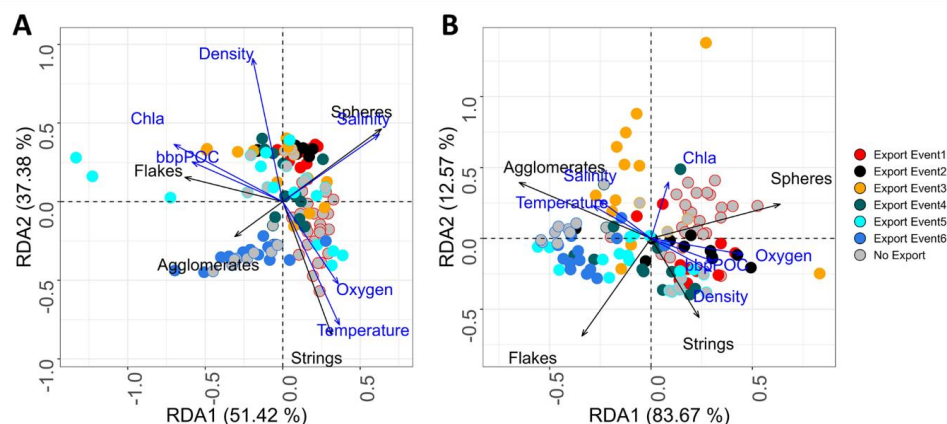
The different marine snow types showed concentrations of similar magnitudes varying from 0 to 20 000 particles m^{-3} . Surface concentrations were two to three fold higher than in the mesopelagic. From May to July 2021, all particle types showed reduced concentrations (in particular in the mesopelagic) compared to the rest of the period which showed an intermittent pattern (Fig. 6). The different particle types shared similar overall spatio-temporal dynamics mainly in the surface but also exhibited distinct features in the deep. In the surface layer and the upper mesopelagic (200-400 m), they all showed concomitant peaks during the bloom periods. In the deeper mesopelagic only agglomerates and spheres showed an increase with a time delay increasing with depth.



345
346 **Figure 6: Contour plot of the four marine snow types: A) Flakes, B) Agglomerate, C) Strings, D) Spheres, as a function**
347 **of time and depth. The 6 export events are depicted by the red vertical dash lines. The black line depicts the 1025.7 kg**
348 **m^{-3} isopycnal. The bathymetry has been overlaid as a white mask.**
349

3.5 Spatio-temporal dynamics of marine snow assemblage

As illustrated in the RDA composite spaces, marine snow assemblages in the surface layer varied with seasons and also between surface and mesopelagic layer (Fig. 7). In the surface layer, contributions to axis 1, reveal the opposite dynamics between spheres and strings compared to flakes and agglomerates. Strings dominate from May to July (before export event 1), spheres from May to October (from export event 1 to export event 3), and agglomerates after February (after export event 5). The first two export events had consistent and homogeneous assemblages dominated by spheres. Subsequent export periods (3, 4, and 5) exhibited varying assemblages, mainly dominated by strings and spheres. The last period (after February) that includes export event 6 differed greatly in the assemblage with a dominance of agglomerates. When comparing periods before and during an export event in the surface layer, apart from the first event, the assemblage did not change. In the deeper layer, the assemblage composition evolution was consistent with the surface one but was more contrasted with less balanced assemblages as indicated by the higher contribution of the first axis (86.9%) relative to the surface (51.6%) (Fig. 7). In the mesopelagic, contributions to this axis reveal the opposite dynamics between spheres compared to flakes and agglomerates. Apart from export event 6, all export events were dominated by spheres. Noticeable is also a more pronounced difference between export events 2 (higher proportion of strings) and 3 (higher proportions of agglomerates and spheres) relative to the surface evolution. Dominance of flakes was not observed.

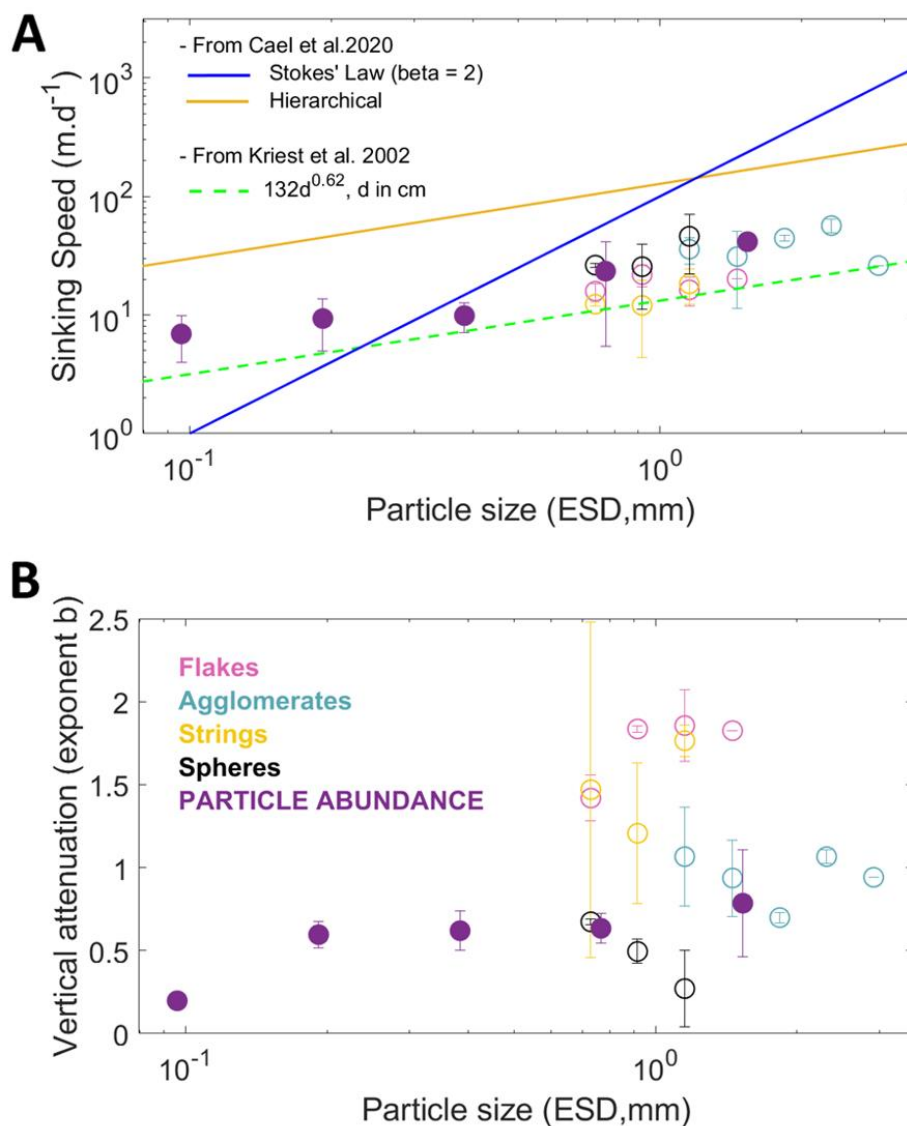


367
 368 **Figure 7 : RDA of marine snow assemblages at each station (dots) A) between 0-100 m (left panel) and B) 400-500 m**
 369 **depth identifying the six periods of export with different colors. Stations observed prior (in gray) to the export event**
 370 **are encircled according to the color of the event. Black arrows show the dominant type of marine snow while the gray**
 371 **arrows show the correlation with environmental variables.**

372 3.6 Sinking speed and vertical attenuation of the plume

373 Sinking speeds, inferred from the lagged correlation between surface and mesopelagic (400-500m)
 374 particle time series, for all types of particles (MiP, MaP, morphotypes 1 to 4) were of 30 m d^{-1} (Supp. Table S2).
 375 By separating the six events and with more size related classification, more details can be obtained to break apart
 376 this constant estimate. However, sinking speeds and attenuation in a plume can only be determined for a given
 377 size range if the abundance variability in the time series is consistent. This was not the case for each size class and
 378 category among the 60 possible cases (6 plumes*10 size ranges from $100 \mu\text{m}$ to 5 mm). Sinking speeds could be
 379 estimated 6 times for flakes, 19 times for agglomerates, 5 times for strings and 12 times for spheres. When
 380 averaging altogether the results from the six export events, a unique size-based relationship is not visible for the
 381 different morphotypes (Fig. 8A), but agglomerates and spheres showed the highest sinking speeds. Also within
 382 the size range for which sinking estimates were possible for all morphotypes (ESD from $1.02\text{-}1.29 \text{ mm}$), spheres
 383 ($46\text{+}/\text{-}24 \text{ m d}^{-1}$) and agglomerates ($35\text{+}/\text{-}9 \text{ m d}^{-1}$) showed higher sinking speeds relative to flakes ($16.29\text{+}/\text{-}4 \text{ m d}^{-1}$)
 384 and strings ($18.33\text{+}/\text{-}6 \text{ m d}^{-1}$) (Table S3). When considering the abundance of all particles $>100 \mu\text{m}$ (MiP+MaP),
 385 sinking speed estimates could be performed in 16 cases (mostly for particles larger than $500 \mu\text{m}$). Sinking speed
 386 increased with size from a minimum of 10 m.d^{-1} to a maximum of 150 m.d^{-1} . It is noticeable that sinking speed
 387 estimation for the largest size classes ($>1.02 \text{ mm}$) was not possible when considering all particles but possible for
 388 agglomerates.

389 The strength of particle abundance attenuation in the plume increased on average with particle size and
 390 showed a remarkable difference between the different morphological types. Spheres had the lowest attenuation
 391 while flakes and strings had the strongest. For spheres, the attenuation decreased as a function of size. For size
 392 class 3, spheres ($0.5\text{+}/\text{-}0.07$) and agglomerates ($0.88\text{+}/\text{-}0.3$) had the lowest attenuation compared to flakes ($1.59\text{+}/\text{-}$
 393 0.02) and string ($1.21\text{+}/\text{-}0.42$) (Table S3). Apart from spheres, for which attenuation decreased significantly with
 394 size, no relationship between attenuation and size was found. Extending the size range by pooling all particles
 395 does not evidence an allometric relationship.



396
 397
 398
 399
 400
 401
 402
 403
 404

Figure 8: Sinking speed versus size (A) and attenuation exponent b versus size (B) for different types of particles averaged for the six different export events. The solid blue line is the Stokes' Law relationship, valid for spherical smooth particles with a constant excess density with increasing size and the orange line is the hierarchical regression on the data compilation in Cael et al., 2021. Dashed green line represents the model parametrizations of size-sinking relationship by (Kriest, 2002).



405

4 DISCUSSION

406

4.1 Hydrological context and ocean circulation during the drift

407

The observed hydrographic characteristics are in general agreement with the seasonal variability of the region. Sea surface temperature, primarily driven by surface heat fluxes, showed the lowest values from July to September and the highest values in March and April (Körner et al., 2023; Scannell and McPhaden, 2018). Sea surface salinity as measured by the float was lowest in November and from March to April. The timing of freshening is in agreement with the seasonal advection of low-salinity waters with the southward-flowing Angola Current (Awo et al., 2022; Kopte et al., 2017). While sea surface temperature shows a dominant annual cycle, upwelling and downwelling near the continental slope are characterized by both an annual and semiannual cycle. Consistent with previous study, the main upwelling season happens during the cold period from July to September while the secondary upwelling season occurs during January to February (Körner et al., 2024). During these periods, float data indicate denser water with minimum oxygen concentrations close to the surface. As there is, in general, good anti-correlation between oxygen and nitrate (Körner et al., 2024), it is possible that during upwelling periods low-oxygen and high-nitrate water enters into the euphotic zone, fueling the six observed production/export events identified in the float data. Periods 1 and 2 are within the main upwelling season and period 5 is during the secondary upwelling season. While period 3 might be during the transition from upwelling to downwelling, periods 4 and 6 were clearly during the secondary and main downwelling seasons, respectively. Note that between April and August 2021 an extreme warm event was present in the Angola basin associated with record low productivity between June and August partly covering the main upwelling season (Imbol Koungue et al., 2024).

425

During the deployment, the float drifted slowly with an average distance between surfacing of 16 km in 3 days. The highest drift (40 km in three days) was observed during periods 3 and 5. ADT shows weak horizontal variability suggesting that the eddy field is present but with low intensity (Fig. 4 in Supp. Mat.). FTLE values generally less than 0.1 d^{-1} indicate weak eddy activity as generally reported in the region (Aguedjou et al., 2019). The negative correlation between all types of particles and FTLE indicates that the bloom events followed by particle accumulation were more intense at low horizontal mixing. The intermittent exports are associated with bloom events that are connected to coastal blooms during periods 4, 5 and to a lesser extent 6. In order to identify the marine snow export plumes (and thus calculate the sinking speeds and vertical attenuation), we made the hypothesis that the water parcel encompassing each plume did not change considerably while the float profiled them. While this Lagrangian assumption cannot be demonstrated with the available data set, different supplementary analyses suggest (Fig. S5, Table S2) that this approximation seems reasonable. The hydrological properties of the mesopelagic, as well as the oxygen concentrations, showed a weak variability during the study period. Low turbulence was observed in the region, as shown by relatively low FTLE values and by the fact that the float did not get trapped in any mesoscale eddy. In addition, previous studies showed a weak vertical shear environment in this region (Kopte et al., 2017). Delayed occurrence in large particle peaks with depth, supports this 1D hypothesis as in previous studies (Briggs et al., 2020; Lacour et al., 2024; Stemmann et al., 2002; Trudnowska et al., 2021) which is not observed in case of strong mesoscale activities (Accardo et al., 2024). A typical mesopelagic nepheloid layer (visible on Bbp and MiP), presumably extending from the seafloor was observed as the float was drifting along the 700 m depth bathymetry. This feature was also observed in the MiP but not in the larger particles (Fig. 4C and 5). Such size differentiated distribution across continental shelves has already been observed elsewhere with combined optical and imaging methods (Durrieu de Madron et al., 1990, 2017). This observation suggests that the nepheloid layers did not contain any large aggregates and therefore did not interfere with our sinking estimates for the large fractions (MaP and the 4 morphotypes) but potentially not for the MiP.

449

4.2 Dynamics of the six marine snow events

450

The four marine snow morphotypes were correlated to *in situ* or remotely sensed Chla suggesting that most of the marine snow was of phytoplanktonic origin (Supp. Fig. S5). Additional material (*i.e.*, phytoplankton in bottles and zooplankton in net) as available in a previous study (Trudnowska et al., 2021) is needed to unambiguously attribute a morphotype to a specific phytoplankton or zooplankton community. However,

453



454 correlation with environmental variables and the shape of particles suggest possible sources of the four types of
455 marine snow. Typical dense fecal pellets, relative to loose marine snow, were not detected by the unsupervised
456 classification but they probably are mostly contained in spheres which contained the most opaque and small
457 particles. Given the observed lower 0-100 m integrated concentration of zooplankton organisms (observed range
458 10^3 - 10^4 ind.m⁻²) relative to marine snow (observed range 10^3 - $20 \cdot 10^4$ ind.m⁻²) as generally found in other studies
459 (Checkley et al., 2008; Forest et al., 2012; Gonzalez-Quiros and Checkley, 2006; Stemmann and Boss, 2012;
460 Trudnowska et al., 2021), it is possible that the contribution of fecal pellets to the total detritus was low. A lower
461 abundance of pellets relative to marine snow was also observed in sediment traps (Durkin et al., 2021) and episodic
462 export of phyto-detritus to the deep is a common feature in many sites (Turner, 2015). The three other categories
463 are probably mostly phytodetritus. It is likely that the two clusters of strings/filaments contained living
464 phytoplankton colonies as they were mostly abundant in the surface water at the time when trichodesmium
465 colonies were detected before the first export event (Supp. Fig. S4). While we acknowledge that the classification
466 in 4 morphotypes may not represent all existing morphological variability, it seems appropriate for our case study.
467 Four to five categories were also useful in other studies (Accardo et al., 2024; Trudnowska et al., 2021). Having
468 four instead of five categories increased the concentration by categories yielding more confidence in estimations
469 of the dynamics of marine snow assemblages, their sinking speeds, and attenuation, while still differentiating the
470 main morphological features of particles. In the future, global compilation of such images together with other
471 phytoplankton and zooplankton variables will allow to refine the number of existing morphotypes.

472 According to the float and satellite observations, the blooms seem to be triggered by different dynamics.
473 Blooms 1, 2, and 3 seem to be associated with typical open ocean upwelling events, as suggested by decreased
474 temperature and oxygen associated with higher Chl_a and Bbp. Conversely, the three other events (and in particular
475 4 and 6) were associated with less salty water. Low salinity is possibly an indicator of coastal input from particle
476 enriched water stemming as far off the Congo river (Brandt et al., 2023). The float was closest to the coast and
477 drifted along it (along the isobath 700 m depth) during period 4. During periods 5 and 6, the float drifted offshore
478 and surface Chl_a showed filaments extending from the coast (Fig. S2), corroborating the hypothesis of coastal
479 inputs. The bloom in period 5 was probably associated with more nutrients as suggested by the rising of the 1025.7
480 kg m⁻³ isopycnal. The sequence of events leading to marine snow accumulation for periods 4 and 6 is less clear as
481 the isopycnal 1025.7 kg m⁻³ was deep and Chl_a biomass was not so high. However, overall significant correlations
482 between temperature, oxygen, density, and all biogeochemical variables (Chl_a, Bbp suspended particles, MiP,
483 MaP, and all zooplankton taxa; (Supp. Fig. S5) suggest that upwelled water triggered an increase in the planktonic
484 production.

485 Apart from the first export event, the different marine snow morphotypes did not change in their relative
486 contribution before and during the export events. The main changes in marine snow assemblages were associated
487 with depth during all events and time (the last event being dominated by agglomerates). The increase with depth
488 of the proportion of spheres is related to a clear reduction in filaments and flakes as previously observed in other
489 systems (Accardo et al., 2024; Trudnowska et al., 2021). These changes suggest that flakes and filaments are less
490 efficiently exported than dense particles even if they are larger in size. Although there were differences between
491 export events in their intensity, the general pattern of marine snow community composition, sinking and
492 attenuation during the first 5 events was the same (Supp. Fig. S6 and S7). Such consistency suggests their
493 production by phytoplankton with a constant community composition unlike the Arctic bloom which showed a
494 succession in primary producers types and marine snow morphotypes (Trudnowska et al., 2021). Contrasting with
495 the first 5 export events, the last export event showed an increased contribution of agglomerates, possibly due to
496 the coastal origin from the Congo river, or due to the most northern location with a different phytoplankton
497 community composition or because aggregation mechanisms may have been different during this event (Sup. Fig.
498 S3). The surface change in the community composition was mirrored in the mesopelagic layer probably resulting
499 from sedimentation. However, sinking speeds, nor attenuation were different from the other events.

500 4.3 Sinking speed and vertical attenuation of different marine snow categories

501 Our sinking speed estimates for 500 µm - 1 mm size range particles (10-50 m d⁻¹) are in the same range
502 as the few other estimates obtained with time series of export plume (Briggs et al., 2020; Lacour et al., 2024;
503 Stemmann et al., 2002; Trudnowska et al., 2021) or obtained with *in situ* devices (Diercks and Asper, 1997;
504 Iversen and Lampitt, 2020; Jouandet et al., 2011; Nowald et al., 2009). However, we calculate smaller sinking



505 speeds relative to other *ex-situ* estimates compiled in previous synthesis as illustrated by the difference between
506 our estimates and the hierarchical regression in the data compilation of (Cael et al., 2021) (Fig. 8). Our sinking
507 estimates are in good agreement with the previous model (Kriest, 2002) which was developed for miscellaneous
508 aggregates. Thus our results confirm that sinking speeds of natural assemblage of marine snow differ from *ex situ*
509 estimates, suggesting that the composition of the particles used in the experiments is biased toward fast sinking
510 particles (Williams and Giering, 2022).

511 Not surprisingly, dense (darker appearances implying denser and more compact structures) marine snow
512 particles (>500 μm) have faster sinking speed than more porous one, a property measured and modeled from
513 experimental works (Giering et al., 2020) but never reported for *in situ* measurement in export plume. The sinking-
514 to-size positive relationship was less obvious for a given aggregate morphotype because of their limited size range.
515 The full size range was covered only for flakes whose sinking speed remained constant with size. However, strings
516 and spheres had increasing sinking speeds with their size. Taken together, these two results confirm that the
517 sinking speed to size relationship may exist for certain types of particles but is not universal (Iversen and Lampitt,
518 2020; Williams and Giering, 2022) as other morphological factors (here density) are at play. Among the different
519 factors (phyto- and zoo- plankton community composition, inorganic ballasting) leading to denser particles
520 (Francois et al., 2002; Guidi et al., 2016; Trudnowska et al., 2021; Turner, 2015), our study indicates
521 phytoplankton aggregates to be principally responsible of the observed stronger export. Extending the size range
522 to 100 μm and pooling all particles together confirms the size-to-sinking relationship with however strong
523 variability between export plumes for the small particles and a limited size range up to the size class 1.0-1.63 mm.
524 For the larger size range, sinking can only be estimated after classification because non-sinking aggregates (flakes
525 and fibers) are dominant at the surface blurring the time series of all particles.

526 Carbon fluxes and their vertical attenuation for the different morphotypes was not calculated because the
527 four categories did not match the few available sizes to POC conversion factors (Alldredge, 1998; Durkin et al.,
528 2021). Instead, export efficiency was addressed from the vertical attenuation of the concentration of the four
529 different categories in the plume. Attenuation varied more with morphotypes than size. For a given size class
530 (1.02-1.29 mm), dense morphotypes (agglomerates and spheres) had the lowest attenuation. The exponent cannot
531 be directly compared to the literature because of the units but also because previous flux attenuation exponent
532 were calculated in a vertical frame in which depth layers are temporarily disconnected (ie, at the time of sampling
533 the surface layer is decoupled from the deep layers) while here we consider the number of particles in the sinking
534 plume as they are consumed by different mesopelagic processes (Giering et al., 2014; Stemmann et al., 2004). We
535 believe that following export plumes provide a more accurate estimation of the attenuation than calculating it from
536 vertical profiles as usually done.

537 Apart from events 4 and 5, we believe that particle spatial gradients in the mesopelagic were low and
538 that the large variability in the sinking speed estimates arise from other methodological factors that are important
539 to discuss to improve further studies. First, the quality of the sinking estimates depend on the abundance of
540 particles *in situ*. Compared to conditions with massive seasonal blooms over a long period of several months
541 (Lacour et al., 2024), the production and export events in the Angola basin were less than 1.5 months with on
542 average 10 times lower concentrations. Both factors yielded a patchy spatial distribution that was smoothed by
543 using a depth bin of 100 m instead of varying depth bin (20 to 200 m) (Lacour et al., 2024). This high variability
544 was amplified as large particles were subdivided in four morphotypes. Second, the deployment in the Angola
545 basin took place close to coastal upwelling systems. Offshore propagating filaments may have had effects on
546 particle vertical distribution mainly on small particles (here Bbp and MiP). Third, the clustering method is not
547 sufficiently selective to obtain homogeneous groups among the aggregates as the overlaps can be seen on the PCA
548 space (Supp. Fig. S1). This non-perfect classification has the effect of smoothing the derived estimates of sinking
549 speed and attenuation.

550
551
552



553 **5 Conclusion**

554 We describe seven bloom events leading to surface accumulation of marine snow based on data obtained
555 from a UVP6 camera mounted on a BGC-Argo float and recovered after one year of deployment. Six of them led
556 to an export event with different types of aggregates and different penetration depths. For the first time, two core
557 parameters for carbon sequestration, sinking speeds, and vertical attenuation, were calculated *in situ* for different
558 sizes and morphotypes. Not all detected marine snow aggregates are sinking despite them being larger than 1 mm.
559 Within a given size range, we show that sinking speeds of porous marine snow are smaller than that of dense
560 marine snow indicating the strong impact of density on sinking speed. However, we show that size is still an
561 important property to determine the sinking speed when considering a larger size range or a specific type of marine
562 snow. Compared to earlier studies which could not distinguish aggregates morphology, the proposed classification
563 allowed us to calculate sinking speeds of millimetric marine snow even in the case when a large fraction of them
564 were not sinking. Compared to published synthesis on marine particles sinking speeds, our *in situ* estimates are
565 consistent with empirical allometric models parameterized for marine aggregates and lower than most *ex situ*
566 estimates posing the question of the impact of the methodology. This study demonstrates the high potential of
567 using cameras on autonomous floats to assess intermittent export following episodic bloom events. To better
568 understand particle dynamics and better assess carbon flux, future works should improve the following key
569 methodological issues, 1) a global library of marine snow images to develop classification algorithm adapted for
570 regional and global applications, 2) size to POC conversion factor for the different types of aggregates, 3) couple
571 BGC-Argo floats with ship surveys to provide more comprehensive contextual data than only those derived from
572 the float and satellite data as in this study, 4) increase acquisition frequency to detect rare larger particles, 5)
573 implement embedded recognition in camera because most of the floats are not recovered.
574

575 **Author Contribution Statement**

576 YDS, LS, RK, designed the study
577 YDS, MB, JH, AB, RL, LS, AA, PB, LD worked on the different components of the data analysis
578 AB calculated the Lagrangian metrics
579 YDS and LS drafted the manuscript
580 All authors reviewed the manuscript.
581

582 **Competing interests**

583 The contact author has declared that none of the authors has any competing interests

584 **Acknowledgment**

585 The authors acknowledge the support of the crew of RV Sonne during cruise SO283 and RV Meteor
586 during cruise M181 for the deployment and recovery of the BGC-Argo float. We are thankful to Marc Picheral
587 and Camille Catalano and the Plateforme d'Imagerie Quantitative de Villefranche (PIQv) to make the UVP6 data
588 available. RK acknowledges funding from the Heisenberg Programme of the German Science Foundation #KI
589 1387/5-1. RK and AB acknowledge support via a "Make Our Planet Great Again" grant of the French National
590 Research Agency within the "Programme d'Investissements d'Avenir"; reference "ANR-19-MPGA-0012". AB,
591 RK, LS, SSp, LD, PB acknowledge support via EU H2020 grant (agreement 817578 TRIATLAS project). AB
592 acknowledges support via "SEASONS" project of the French National Center of Spatial Studies (CNES). LD
593 acknowledges support via Sorbonne Université through the Ecole doctorale 129.
594 YDS acknowledges support via "Make Our Planet Great Again" visiting fellowship program for early career
595 researchers and granted by the French Ministry for Europe and Foreign Affairs, in collaboration with the French
596 Ministry for Higher Education and Research, and implemented by Campus France.
597
598



599 **Bibliography**

- 600 Accardo, A., Laxenaire, R., Baudena, A., Speich, S., Kiko, R., and Stemmann, L.: Massive and localized export
601 of selected marine snow types at eddy edges in the South Atlantic Ocean, *EGUsphere*, 2024, 1–29, 2024.
- 602 Aguedjou, H., Dadou, I., Chaigneau, A., Morel, Y., and Alory, G.: Eddies in the Tropical Atlantic Ocean and
603 their seasonal variability, *Geophysical Research Letters*, 46, 12156–12164, 2019.
- 604 Alldredge, A.: The carbon, nitrogen and mass content of marine snow as a function of aggregate size, *Deep-Sea
605 Research Part I-Oceanographic Research Papers*, 45, 529–541, 1998.
- 606 Alldredge, A. L. and Gotschalk, C.: In situ settling behavior of marine snow, *Limnology and Oceanography*, 33,
607 339–351, 1988.
- 608 Alldredge, A. L. and Silver, M. W.: Characteristics, dynamics and significance of marine snow, *Prog.
609 Oceanogr.*, 20, 41–82, 1988.
- 610 Awo, F. M., Rouault, M., Ostrowski, M., Tomety, F. S., Da-Allada, C. Y., and Jouanno, J.: Seasonal cycle of
611 sea surface salinity in the Angola Upwelling System, *Journal of Geophysical Research: Oceans*, 127,
612 e2022JC018518, 2022.
- 613 Baudena, A., Ser-Giacomi, E., D’Onofrio, D., Capet, X., Cotté, C., Cherel, Y., and D’Ovidio, F.: Fine-scale
614 structures as spots of increased fish concentration in the open ocean. *Sci Rep* 11: 15805, 2021.
- 615 Biard, T., Stemmann, L., Picheral, M., Mayot, N., Vandromme, P., Hauss, H., Gorsky, G., Guidi, L., Kiko, R.,
616 and Not, F.: In situ imaging reveals the biomass of giant protists in the global ocean, *Nature*, 532, 504+,
617 <https://doi.org/10.1038/nature17652>, 2016.
- 618 Boyd, P. W., Claustre, H., Levy, M., Siegel, D. A., and Weber, T.: Multi-faceted particle pumps drive carbon
619 sequestration in the ocean, *Nature*, 568, 327–335, 2019.
- 620 Brandt, P., Alory, G., Awo, F. M., Dengler, M., Djakouré, S., Imbol Koungue, R. A., Jouanno, J., Körner, M.,
621 Roch, M., and Rouault, M.: Physical processes and biological productivity in the upwelling regions of the
622 tropical Atlantic, *Ocean Science*, 19, 581–601, 2023.
- 623 Briggs, N., Dall’Olmo, G., and Claustre, H.: Major role of particle fragmentation in regulating biological
624 sequestration of CO₂ by the oceans, *Science*, 367, 791–+, <https://doi.org/10.1126/science.aay1790>, 2020.
- 625 Burd, A. B.: Modeling the Vertical Flux of Organic Carbon in the Global Ocean, *Annual review of marine
626 science*, 16, 2023.
- 627 Burd, A. B., Hansell, D. A., Steinberg, D. K., Anderson, T. R., Aristegui, J., Baltar, F., Beaupre, S. R.,
628 Buesseler, K. O., DeHairs, F., Jackson, G. A., Kadko, D. C., Koppelman, R., Lampitt, R. S., Nagata, T.,
629 Reinthaler, T., Robinson, C., Robison, B. H., Tamburini, C., and Tanaka, T.: Assessing the apparent imbalance
630 between geochemical and biochemical indicators of meso- and bathypelagic biological activity: What the @!\$#
631 is wrong with present calculations of carbon budgets?, *Deep-Sea Research Part II-Topical Studies in
632 Oceanography*, 57, 1557–1571, <https://doi.org/10.1016/j.dsr2.2010.02.022>, 2010.
- 633 Cael, B., Cavan, E. L., and Britten, G. L.: Reconciling the size-dependence of marine particle sinking speed,
634 *Geophysical Research Letters*, 48, e2020GL091771, 2021.
- 635 Chambault, P., Baudena, A., Bjorndal, K. A., Santos, M. A., Bolten, A. B., and Vandeperre, F.: Swirling in the
636 ocean: Immature loggerhead turtles seasonally target old anticyclonic eddies at the fringe of the North Atlantic
637 gyre, *Progress in Oceanography*, 175, 345–358, 2019.
- 638 Checkley, D. M., Davis, R. E., Herman, A. W., Jackson, G. A., Beanlands, B., and Regier, L. A.: Assessing
639 plankton and other particles in situ with the SOLOPC, *Limnology and Oceanography*, 53, 2123–2136, 2008.
- 640 Diercks, A. R. and Asper, V. L.: In situ settling speeds of marine snow aggregates below the mixed layer: Black
641 Sea and Gulf of Mexico, *Deep-Sea Research Part I-Oceanographic Research Papers*, 44, 385–398, 1997.
- 642 Drago, L., Panaiotis, T., Irisson, J.-O., Babin, M., Biard, T., Carlotti, F., Coppola, L., Guidi, L., Hauss, H.,
643 Karp-Boss, L., Lombard, F., McDonnell, A. M. P., Picheral, M., Rogge, A., Waite, A. M., Stemmann, L., and
644 Kiko, R.: Global Distribution of Zooplankton Biomass Estimated by In Situ Imaging and Machine Learning,
645 *FRONTIERS IN MARINE SCIENCE*, 9, <https://doi.org/10.3389/fmars.2022.894372>, 2022.
- 646 Durkin, C. A., Buesseler, K. O., Cetinić, I., Estapa, M. L., Kelly, R. P., and Omand, M.: A visual tour of carbon
647 export by sinking particles, *Global Biogeochemical Cycles*, 35, e2021GB006985, 2021.
- 648 Durrieu de Madron, X., Nyffeler, F., and Godet, C. H.: Hydrographic structure and nepheloid spatial distribution
649 in the Gulf of Lions continental margin, *Continental Shelf Research*, 10, 915–929, 1990.
- 650 Durrieu de Madron, X., Ramondenc, S., Berline, L., Houpert, L., Bosse, A., Martini, S., Guidi, L., Conan, P.,
651 Curtil, C., and Delsaut, N.: Deep sediment resuspension and thick nepheloid layer generation by open-ocean
652 convection, *Journal of Geophysical Research: Oceans*, 122, 2291–2318, 2017.
- 653 Forest, A., Stemmann, L., Picheral, M., Burdorf, L., Robert, D., Fortier, L., and Babin, M.: Size distribution of
654 particles and zooplankton across the shelf-basin system in southeast Beaufort Sea: combined results from an
655 Underwater Vision Profiler and vertical net tows, *Biogeosciences*, 9, 1301–1320, <https://doi.org/10.5194/Bg-9-1301-2012>, 2012.
- 656 Forest, A., Babin, M., Stemmann, L., Picheral, M., Sampei, M., Fortier, L., Gratton, Y., Belanger, S., Devred,
657 E., Sahlin, J., Doxaran, D., Joux, F., Ortega-Retuerta, E., Martin, J., Jeffrey, W. H., Gasser, B., and Miquel, J.



- 659 C.: Ecosystem function and particle flux dynamics across the Mackenzie Shelf (Beaufort Sea, Arctic Ocean): an
660 integrative analysis of spatial variability and biophysical forcings, *Biogeosciences*, 10, 2833–2866,
661 <https://doi.org/10.5194/bg-10-2833-2013>, 2013.
- 662 Francois, R., Honjo, S., Krishfield, R., and Manganini, S.: Factors controlling the flux of organic carbon to the
663 bathypelagic zone of the ocean, *Global Biogeochem. Cycles*, 16, [doi:10.1029/2001GB001722], 2002.
- 664 Giering, S. L. C., Richard Sanders, Richard S. Lampitt, Thomas R. Anderson, Christian Tamburini, Mehdi
665 Boutrif, Mikhail V. Zubkov, Chris M. Marsay, Stephanie A. Henson, Kevin Saw, Kathryn Cook, and Daniel J.
666 Mayor: Reconciliation of the carbon budget in the ocean’s twilight zone, *Nature*, 507, 17,
667 <https://doi.org/10.1038/nature13123>, 2014.
- 668 Giering, S. L. C., Cavan, E. L., Basedow, S. L., Briggs, N., Burd, A. B., Darroch, L. J., Guidi, L., Irisson, J. O.,
669 Iversen, M. H., Kiko, R., Lindsay, D., Marcolin, C. R., McDonnell, A. M. P., Moller, K. O., Passow, U.,
670 Thomalla, S., Trull, T. W., and Waite, A. M.: Sinking Organic Particles in the Ocean-Flux Estimates From in
671 situ Optical Devices, *Frontiers in Marine Science*, 6, <https://doi.org/10.3389/fmars.2019.00834>, 2020.
- 672 Gonzalez-Quiros, R. and Checkley, D. M.: Occurrence of fragile particles inferred from optical plankton
673 counters used in situ and to analyze net samples collected simultaneously, *Journal of Geophysical Research-*
674 *Oceans*, 111, 2006.
- 675 Gorsky, G., Picheral, M., and Stemann, L.: Use of the Underwater Video Profiler for the study of aggregate
676 dynamics in the North Mediterranean, *Estuarine Coastal and Shelf Science*, 50, 121–128, 2000.
- 677 Guidi, L., Jackson, G. A., Stemann, L., Miquel, J. C., Picheral, M., and Gorsky, G.: Relationship between
678 particle size distribution and flux in the mesopelagic zone, *Deep Sea Research Part I: Oceanographic Research*
679 *Papers*, 55, 1364–1374, <https://doi.org/10.1016/j.dsr.2008.05.014>, 2008.
- 680 Guidi, L., Legendre, L., Reygondeau, G., Uitz, J., Stemann, L., and Henson, S. A.: A new look at ocean
681 carbon remineralization for estimating deepwater sequestration, *Global Biogeochem. Cycles*, 29, 1044–1059,
682 <https://doi.org/10.1002/2014gb005063>, 2015.
- 683 Guidi, L., Chaffron, S., Bittner, L., Eveillard, D., Larhlimi, A., Roux, S., Darzi, Y., Audic, S., Berline, L., Brum,
684 J. R., Coelho, L. P., Espinoza, J. C. L., Malviya, S., Sunagawa, S., Dimier, C., Kandels-Lewis, S., Picheral, M.,
685 Poulain, J., Searson, S., Stemann, L., Not, F., Hingamp, P., Speich, S., Follows, M., Karp-Boss, L., Boss, E.,
686 Ogata, H., Pesant, S., Weissenbach, J., Wincker, P., Acinas, S. G., Bork, P., de Vargas, C., Iudicone, D.,
687 Sullivan, M. B., Raes, J., Karsenti, E., Bowler, C., Gorsky, G., and Tara Oceans Consortium Coordinator:
688 Plankton networks driving carbon export in the oligotrophic ocean, *Nature*, 532, 465–+, 2016.
- 689 Henson, S., Bisson, K., Hammond, M., Martin, A., Mouw, C., and Yool, A.: Effect of sampling bias on global
690 estimates of ocean carbon export, *Environmental Research Letters*, 2024.
- 691 Honjo, S., Manganini, S. J., and Cole, J. J.: Sedimentation of biogenic matter in the deep ocean, *Deep-Sea*
692 *Research*, 29, 609–625, 1982.
- 693 Imbol Koungue, R. A., Brandt, P., Prigent, A., Aroucha, L. C., Lübbecke, J., Imbol Nkwinkwa, A. S. N.,
694 Dengler, M., and Keenlyside, N.: Drivers and impact of the 2021 extreme warm event in the tropical Angolan
695 upwelling system, *Scientific Reports*, 14, 16824, 2024.
- 696 Irisson, J.-O., Ayata, S.-D., Lindsay, D. J., Karp-Boss, L., and Stemann, L.: Machine Learning for the Study
697 of Plankton and Marine Snow from Images., *Annual review of marine science*, 14, 277–301,
698 <https://doi.org/10.1146/annurev-marine-041921-013023>, 2022.
- 699 Iversen, M. H. and Lampitt, R. S.: Size does not matter after all: no evidence for a size-sinking relationship for
700 marine snow, *Progress in Oceanography*, 189, 102445, 2020.
- 701 Iversen, M. H., Nowald, N., Ploug, H., Jackson, G. A., and Fischer, G.: High resolution profiles of vertical
702 particulate organic matter export off Cape Blanc, Mauritania: Degradation processes and ballasting effects,
703 *Deep-Sea Research Part I-Oceanographic Research Papers*, 57, 771–784,
704 <https://doi.org/10.1016/j.dsr.2010.03.007>, 2010.
- 705 Jackson, G. A. and Checkley, D. M.: Particle size distributions in the upper 100 m water column and their
706 implications for animal feeding in the plankton, *Deep-Sea Research Part I-Oceanographic Research Papers*, 58,
707 283–297, <https://doi.org/10.1016/j.dsr.2010.12.008>, 2011.
- 708 Jouandet, M.-P., Trull, T. W., Guidi, L., Picheral, M., Ebersbach, F., Stemann, L., and Blain, S.: Optical
709 imaging of mesopelagic particles indicates deep carbon flux beneath a natural iron-fertilized bloom in the
710 Southern Ocean, *Limnology and Oceanography*, 56, 1130–1140, <https://doi.org/10.4319/lo.2011.56.3.1130>,
711 2011.
- 712 Kiko, R., Biastoch, A., Brandt, P., Cravatte, S., Hauss, H., Hummels, R., Kriest, I., Marin, F., McDonnell, A. M.
713 P., Oschlies, A., Picheral, M., Schwarzkopf, F. U., Thurnherr, A. M., and Stemann, L.: Biological and
714 physical influences on marine snowfall at the equator, *Nature Geoscience*, 10, 852–+,
715 <https://doi.org/10.1038/ngeo3042>, 2017.
- 716 Kiko, R., Brandt, P., Christiansen, S., Faustmann, J., Kriest, I., Rodrigues, E., Schütte, F., and Hauss, H.:
717 Zooplankton-mediated fluxes in the eastern tropical North Atlantic, *Frontiers in Marine Science*, 7, 358, 2020.
- 718 Kopte, R., Brandt, P., Dengler, M., Tchupalanga, P., Macuéria, M., and Ostrowski, M.: The Angola C current:



- 719 Flow and hydrographic characteristics as observed at 11° S, *Journal of Geophysical Research: Oceans*, 122,
720 1177–1189, 2017.
- 721 Körner, M., Brandt, P., and Dengler, M.: Seasonal cycle of sea surface temperature in the tropical Angolan
722 Upwelling System, *Ocean Science*, 19, 121–139, 2023.
- 723 Körner, M., Brandt, P., Illig, S., Dengler, M., Subramaniam, A., Bachèlery, M.-L., and Krahnemann, G.: Coastal
724 trapped waves and tidal mixing control primary production in the tropical Angolan upwelling system, *Science
725 Advances*, 10, eadj6686, 2024.
- 726 Kriest, I.: Different parameterizations of marine snow in a 1D-model and their influence on representation of
727 marine snow, nitrogen budget and sedimentation, *Deep Sea Research Part I: Oceanographic Research Papers*,
728 49, 2133–2162, 2002.
- 729 Kriest, I. and Evans, G. T.: A vertically resolved model for phytoplankton aggregation, *Proceedings of the
730 Indian Academy of Sciences-Earth & Planetary Sciences*, 109, 453–469, 2000.
- 731 Lacour, L., Briggs, N., Petiteau, L., Bressac, M., Guidi, L., Castro, B. F., Picheral, M., Catalano, C.,
732 Schmechtig, C., and Leymarie, E.: Particle size sets the carbon penetration depth during ocean bloom export
733 events, 2024.
- 734 Laget, M., Drago, L., Panaïotis, T., Kiko, R., Stemmann, L., Rogge, A., Llopis-Monferrer, N., Leynaert, A.,
735 Irisson, J.-O., and Biard, T.: Global census of the significance of giant mesopelagic protists to the marine carbon
736 and silicon cycles, *Nature Communications*, 15, 3341, 2024.
- 737 Laurenceau-Cornec, E. C., Trull, T. W., Davies, D. M., Christina, L., and Blain, S.: Phytoplankton morphology
738 controls on marine snow sinking velocity, *Marine Ecology Progress Series*, 520, 35–56, 2015.
- 739 Legendre, P. and Legendre, L.: Chapter 11 - Canonical analysis, in: *Developments in Environmental Modelling*,
740 vol. 24, edited by: Legendre, P. and Legendre, L., Elsevier, 625–710, [https://doi.org/10.1016/B978-0-444-
741 53868-0.50011-3](https://doi.org/10.1016/B978-0-444-53868-0.50011-3), 2012.
- 742 Martin, J. H., Knauer, G. A., Karl, D. M., and Broenkow, W. W.: VERTEX: carbon cycling in the northeast
743 Pacific, *Deep Sea Research Part A. Oceanographic Research Papers*, 34, 267–285, 1987.
- 744 McDonnell, A. M. P. and Buesseler, K. O.: Variability in the average sinking velocity of marine particles,
745 *Limnology and Oceanography*, 55, 2085–2096, <https://doi.org/10.4319/lo.2010.55.5.2085>, 2010.
- 746 McInnes, L., Healy, J., and Melville, J.: Umap: Uniform manifold approximation and projection for dimension
747 reduction, *arXiv preprint arXiv:1802.03426*, 2018.
- 748 Nowald, N., Fischer, G., Rattmeyer, V., Iversen, M., Reuter, C., Wefer, G., and Ieee: In-situ sinking speed
749 measurements of marine snow aggregates acquired with a settling chamber mounted to the Cherokee ROV, in:
750 *Oceans 2009 - Europe, Vols 1 and 2*, 1286–1291, 2009.
- 751 Panaïotis, T., Babin, M., Biard, T., Carlotti, F., Coppola, L., Guidi, L., Hauss, H., Karp-Boss, L., Kiko, R.,
752 Lombard, F., McDonnell, A. M. P., Picheral, M., Rogge, A., Waite, A. M., Stemmann, L., and Irisson, J.-O.:
753 Three major mesoplanktonic communities resolved by in situ imaging in the upper 500 m of the global ocean,
754 *GLOBAL ECOLOGY AND BIOGEOGRAPHY*, <https://doi.org/10.1111/geb.13741>, 2023.
- 755 Picheral, M., Guidi, L., Stemmann, L., Karl, D. M., Iddaoud, G., and Gorsky, G.: The Underwater Vision
756 Profiler 5: An advanced instrument for high spatial resolution studies of particle size spectra and zooplankton,
757 *Limnology and Oceanography-Methods*, 8, 462–473, <https://doi.org/10.4319/lom.2010.8.462>, 2010.
- 758 Picheral, M., Catalano, C., Brousseau, D., Claustre, H., Coppola, L., Leymarie, E., Coindat, J., Dias, F., Fevre,
759 S., Guidi, L., Irisson, J. O., Legendre, L., Lombard, F., Mortier, L., Penkerch, C., Rogge, A., Schmechtig, C.,
760 Thibault, S., Tixier, T., Waite, A., and Stemmann, L.: The Underwater Vision Profiler 6: an imaging sensor of
761 particle size spectra and plankton, for autonomous and cabled platforms, *LIMNOLOGY AND
762 OCEANOGRAPHY-METHODS*, 20, 115–129, <https://doi.org/10.1002/lom3.10475>, 2022.
- 763 Ploug, H., Iversen, M. H., and Fischer, G.: Ballast, sinking velocity, and apparent diffusivity within marine
764 snow and zooplankton fecal pellets: Implications for substrate turnover by attached bacteria, *Limnology and
765 Oceanography*, 53, 1878–1886, 2008a.
- 766 Ploug, H., Iversen, M. H., Koski, M., and Buitenhuis, E. T.: Production, oxygen respiration rates, and sinking
767 velocity of copepod fecal pellets: Direct measurements of ballasting by opal and calcite, *Limnology and
768 Oceanography*, 53, 469–476, 2008b.
- 769 Ploug, H., Terbruggen, A., Kaufmann, A., Wolf-Gladrow, D., and Passow, U.: A novel method to measure
770 particle sinking velocity in vitro, and its comparison to three other in vitro methods, *Limnology and
771 Oceanography-Methods*, 8, 386–393, <https://doi.org/10.4319/lom.2010.8.386>, 2010.
- 772 Scannell, H. A. and McPhaden, M. J.: Seasonal mixed layer temperature balance in the southeastern tropical
773 Atlantic, *Journal of Geophysical Research: Oceans*, 123, 5557–5570, 2018.
- 774 Ser-Giacomi, E., Baudena, A., Rossi, V., Follows, M., Clayton, S., Vasile, R., López, C., and Hernández-García,
775 E.: Lagrangian betweenness as a measure of bottlenecks in dynamical systems with oceanographic examples,
776 *Nature communications*, 12, 4935, 2021.
- 777 Shadden, S. C., Lekien, F., and Marsden, J. E.: Definition and properties of Lagrangian coherent structures from
778 finite-time Lyapunov exponents in two-dimensional aperiodic flows, *Physica D: Nonlinear Phenomena*, 212,



- 779 271–304, 2005.
- 780 Siegel, D. A., DeVries, T., Cetinić, I., and Bisson, K. M.: Quantifying the Ocean’s Biological Pump and Its
781 Carbon Cycle Impacts on Global Scales, *Annual review of marine science*, 15, 329–356, 2023.
- 782 Soviadan, Y. D., Benedetti, F., Brandão, M. C., Ayata, S.-D., Irisson, J.-O., Jamet, J. L., Kiko, R., Lombard, F.,
783 Gnanadi, K., and Stemmann, L.: Patterns of mesozooplankton community composition and vertical fluxes in the
784 global ocean, *Progress in Oceanography*, 200, 102717, <https://doi.org/10.1016/j.pocean.2021.102717>, 2022.
- 785 Stemmann, L. and Boss, E.: Plankton and Particle Size and Packaging: From Determining Optical Properties to
786 Driving the Biological Pump, *Annu Rev Mar Sci*, 4, 263–290, <https://doi.org/Doi.10.1146/Annurev-Marine-120710-100853>, 2012.
- 787 Stemmann, L., Gorsky, G., Marty, J. C., Picheral, M., and Miquel, J. C.: Four-year study of large-particle
788 vertical distribution (0–1000 m) in the NW Mediterranean in relation to hydrology, phytoplankton, and vertical
789 flux, *Deep-Sea Research Part II-Topical Studies in Oceanography*, 49, 2143–2162, 2002.
- 790 Stemmann, L., Jackson, G. A., and Gorsky, G.: A vertical model of particle size distributions and fluxes in the
791 midwater column that includes biological and physical processes - Part II: application to a three year survey in
792 the NW Mediterranean Sea, *Deep-Sea Research Part I-Oceanographic Research Papers*, 51, 885–908,
793 <https://doi.org/10.1016/j.dsr.2004.03.002>, 2004.
- 794 Stemmann, L., Youngbluth, M., Robert, K., Hosia, A., Picheral, M., Paterson, H., Ibanez, F., Guidi, L.,
795 Lombard, F., and Gorsky, G.: Global zoogeography of fragile macrozooplankton in the upper 100–1000 m
796 inferred from the underwater video profiler, *Ices Journal of Marine Science*, 65, 433–442,
797 <https://doi.org/10.1093/icesjms/fsn010>, 2008.
- 798 Stolarek, I., Samelak-Czajka, A., Figlerowicz, M., and Jackowiak, P.: Dimensionality reduction by UMAP for
799 visualizing and aiding in classification of imaging flow cytometry data, *iScience*, 25, 105142,
800 <https://doi.org/10.1016/j.isci.2022.105142>, 2022.
- 801 Teixeira, J., Rocha, V., Oliveira, J., Jorge, P. A. S., and Silva, N. A.: Towards real-time identification of trapped
802 particles with UMAP-based classifiers, *J. Phys.: Conf. Ser.*, 2407, 012043, <https://doi.org/10.1088/1742-6596/2407/1/012043>, 2022.
- 803 Trudnowska, E., Lacour, L., Ardyna, M., Rogge, A., Irisson, J. O., Waite, A. M., Babin, M., and Stemmann, L.:
804 Marine snow morphology illuminates the evolution of phytoplankton blooms and determines their subsequent
805 vertical export., *Nature communications*, 12, 2816–2816, <https://doi.org/10.1038/s41467-021-22994-4>, 2021.
- 806 Turner, J. T.: Zooplankton fecal pellets, marine snow, phytodetritus and the ocean’s biological pump, *Progress*
807 *in Oceanography*, 130, 205–248, 2015.
- 808 Volk, T. and Hoffert, M. I.: Ocean carbon pumps: analysis of relative strengths and efficiencies in ocean-driven
809 atmospheric CO₂ changes, in: *The Carbon Cycle and Atmospheric CO₂: Natural Variations Archean to Present*,
810 vol. 32, edited by: Sundquist, E. T. and Broecker, W. S., Washington, D.C, 99–110, 1985.
- 811 Williams, J. and Giering, S.: In situ particle measurements deemphasize the role of size in governing the sinking
812 velocity of marine particles, *Geophysical Research Letters*, 49, e2022GL099563, 2022.
- 813 Yeo, I. and Johnson, R. A.: A new family of power transformations to improve normality or symmetry,
814 *Biometrika*, 87, 954–959, <https://doi.org/10.1093/biomet/87.4.954>, 2000.